Supplementary material

Synergistic Defect- and Interface-Engineering of Bi_2S_3-based Nanowall Network High-Performance Photoelectrochemical Solar Water Splitting

Ying Wang,[a] Min Liu,[b] Shiqiang Hao,[c] Yuan Li,[d,e,] Qianqian Li,[f] Fangyang Liu,[a] Yanqing Lai,[a] Jie Li,[a] Chris Wolverton,[c] Vinayak P. Dravid,[c] Liangxing Jiang[a,]**

[a.] *School of Metallurgy and Environment, Central South University, Changsha, Hunan 410083, China*

[b.] *School of physics and electronics, Central South University, Changsha, Hunan 410083, China*

[c.] *Northwestern University Atomic and Nanoscale Characterization Experimental (NUANCE) Centre, Department of Materials Science and Engineering, Northwestern University, Evanston, Illinois 60208, USA*

[d.] *State Key Laboratory of Material Processing and Die & Mould Technology, School of Materials Science and Engineering, Huazhong University of Science and Technology, Wuhan, Hubei 430074, China*

[e.] *Shenzhen Huazhong University of Science and Technology Research Institute, Shenzhen 518057, China.*

[f.] *Materials Genome Institute, Shanghai University, Shanghai 200444, China*

S1. Supplementary Tables

Table S1. The lengths of Bi-O and Bi-S bonds and coordination numbers of Bi atom are extracted from the curve-fitting. CN, the coordination numbers of Bi atom; R, the lengths of Bi-O and Bi-S bonds; ss, the Debye-Waller factor.

sample	EXAFS	bond	CN	R(Å)	ss
i-Bi_2S_3	Bi L3	Bi-O	0.52	2.2199	0.0001
		Bi-S	2.8	2.6117	0.005
v-Bi_2S_3	Bi L3	Bi-O	0.4	2.1599	0.00008
		Bi-S	2.44	2.6267	0.0044
v-Bi_2S_3/Co_3O_4	Bi L3	Bi-O	0.5	2.1799	0.000005
		Bi-S	2.96	2.6117	0.00545

S2. Supplementary Figures

Fig. S1. Morphology-inheritable multi-step thermal annealing process. (a-c) SEM images of the top surface (a,b) and cross-section (c) of the pristine Bi_2O_3 nanowall network. (d-f) SEM images of the top surface (d,e) and cross-section (f) of the native *i*-Bi_2S_3. (g-i) SEM images of the top surface (g,h) and cross-section (i) of the defective *v*-Bi_2S_3. (j-l) SEM images of the top surface (j,k) and cross-section (l) of the final *v*-Bi_2S_3/Co_3O_4 heterostructures.

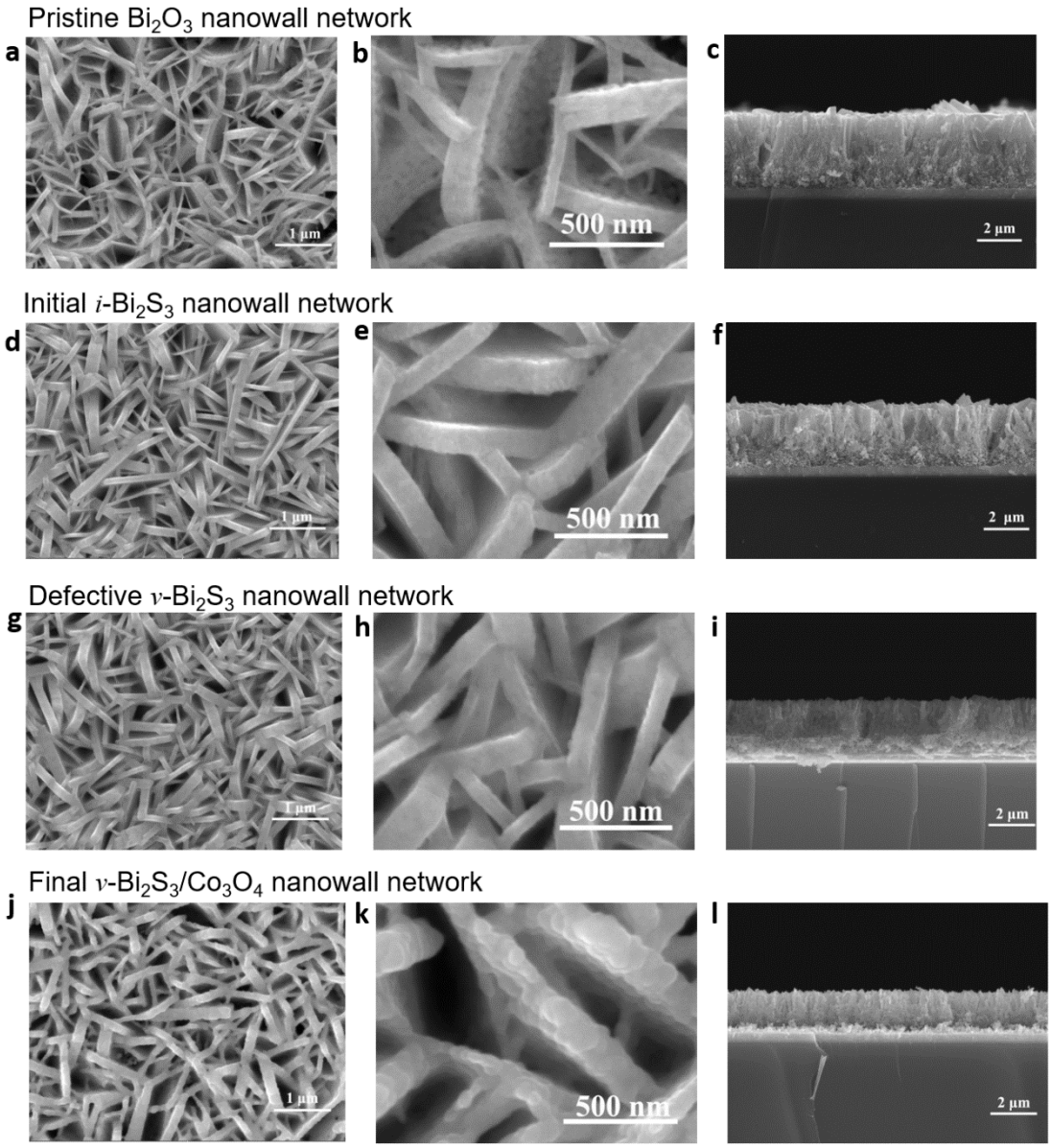

Fig. S2. Morphology for *v*-Bi_2S_3 with different post-annealing time. (a) 0 min (b) 15 min (c) 30 min (d)45 min.

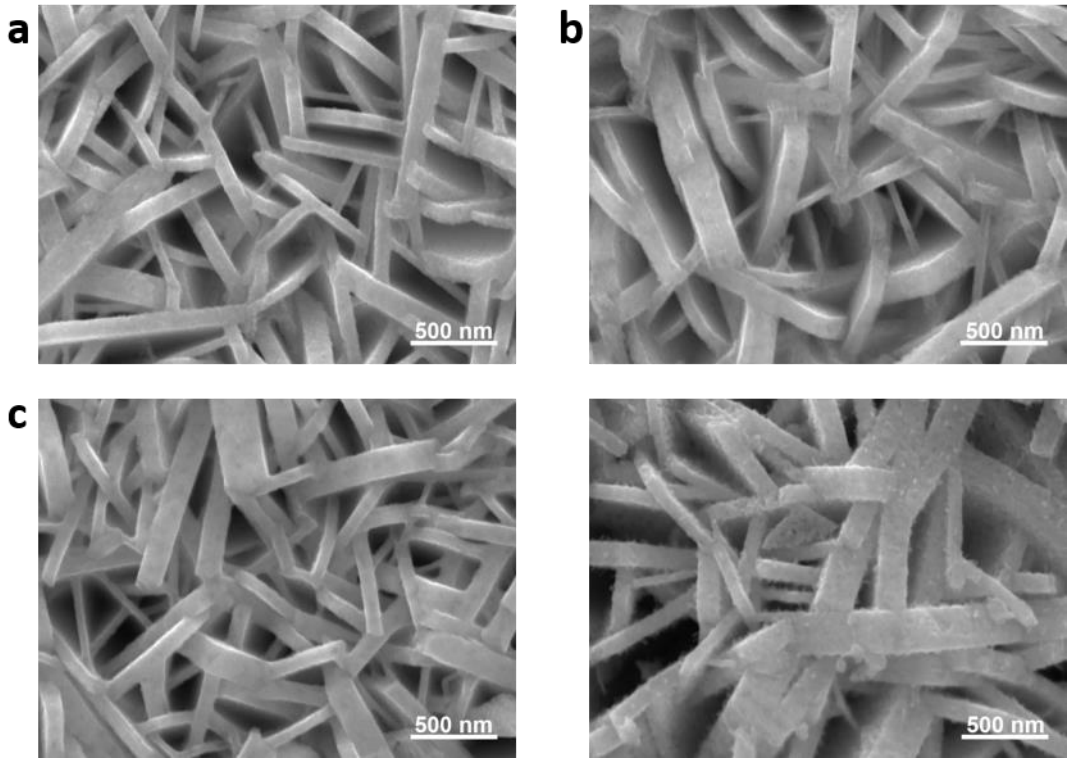

Fig. S3. (a) XRD and (b) PEC performance for *v*-Bi_2S_3 with different post-annealing time.

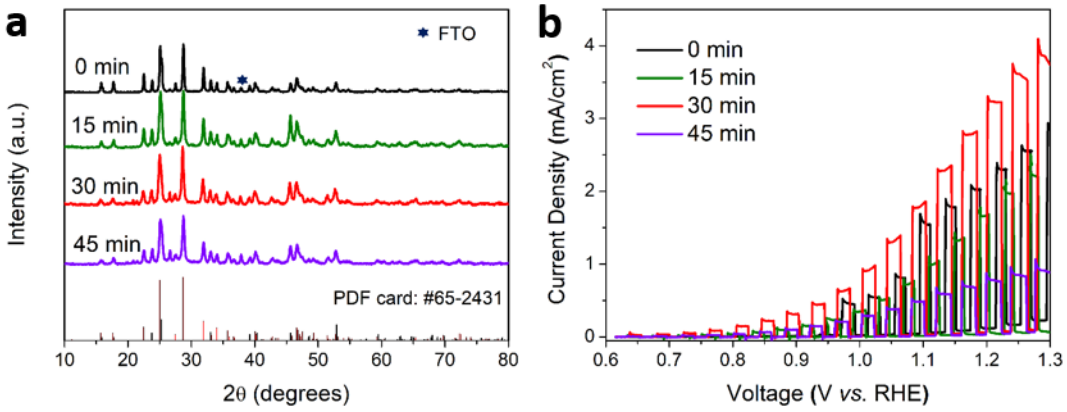

Fig. S4. Fitted result of EXAFS spectra. (a) initial Bi_2S_3 (*i*-Bi_2S_3), (b) the vacancy-rich Bi_2S_3 (*v*-Bi_2S_3), and (c) the final *v*-Bi_2S_3/Co_3O_4 heterostructure. Blue and red lines represent experimental and fitting curves, respectively.

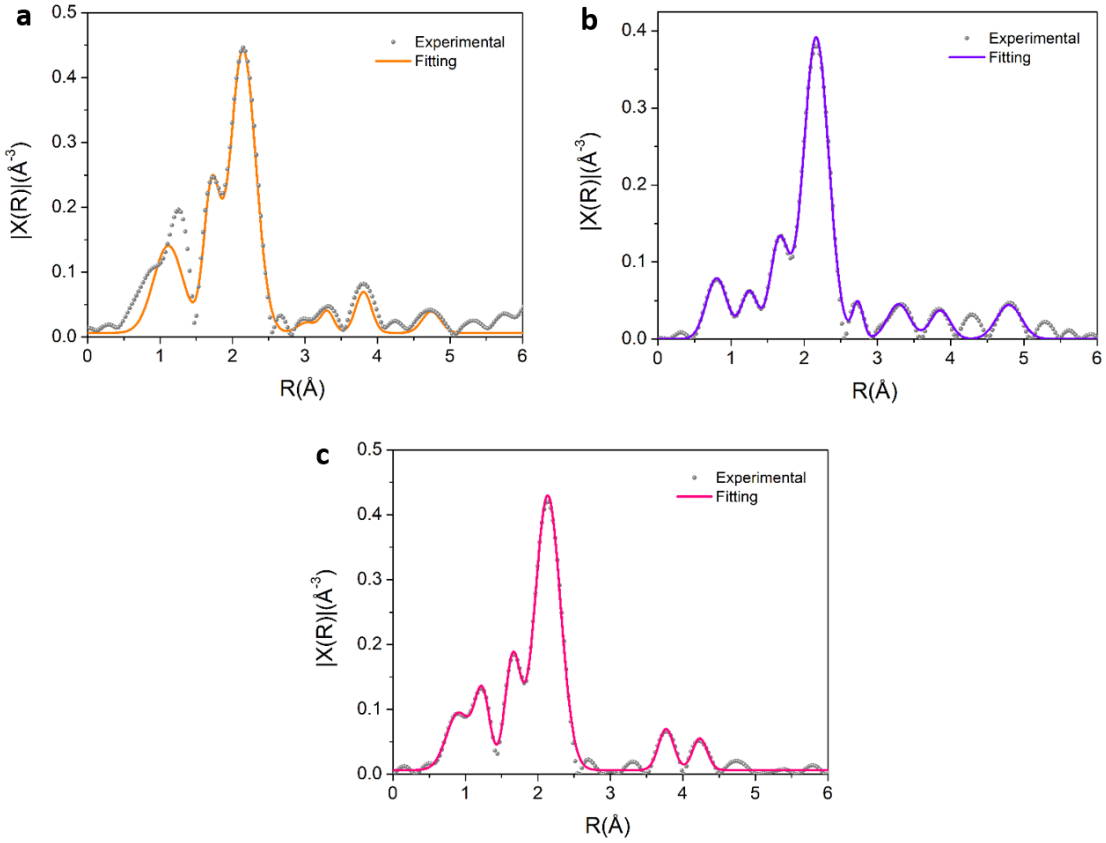

Fig. S5. (a) the absorbance spectra, (b) Raman spectra, (c) Electron spin resonance EPR spectra and (d) the XPS spectra of O 1s for initial Bi_2S_3 (*i*-Bi_2S_3), the vacancy-rich Bi_2S_3 (*v*-Bi_2S_3), and the final *v*-Bi_2S_3/Co_3O_4 heterostructure.

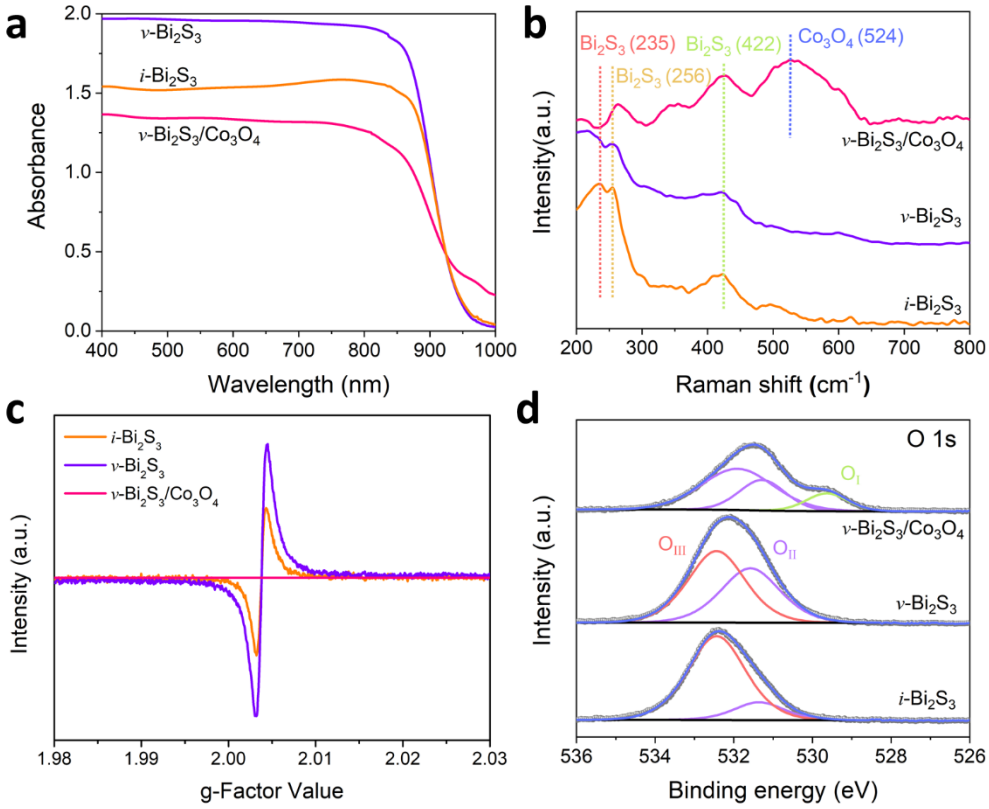

Fig. S6. (a) Mott–Schottky plots under dark conditions and (b) UPS spectra of initial Bi_2S_3 (*i*-Bi_2S_3), the vacancy-rich Bi_2S_3 (*v*-Bi_2S_3), and the final *v*-Bi_2S_3/Co_3O_4 heterostructure. The green dashed lines indicate the area shown in the zoomed-in image in the inset.

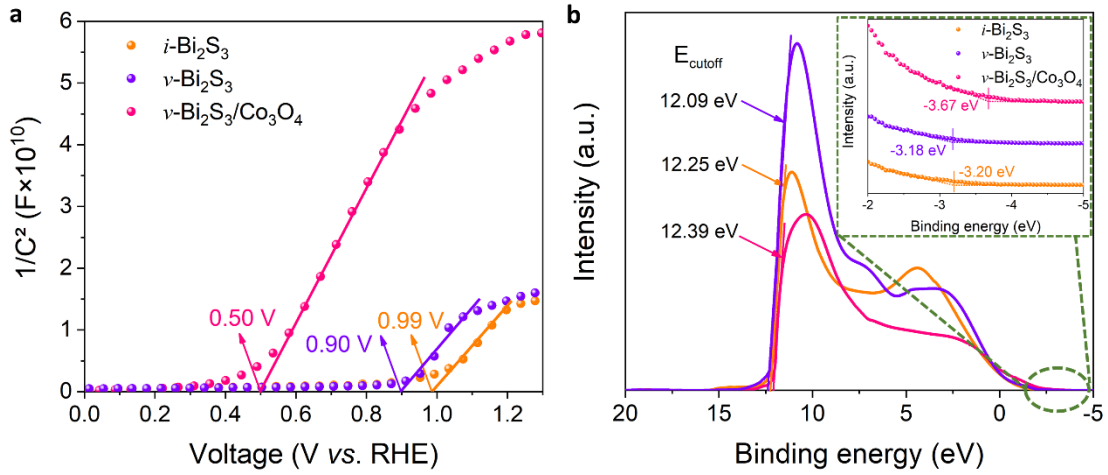

Fig. S7. Current-potential curves for the *i*-Bi_2S_3, *v*-Bi_2S_3, and *v*-Bi_2S_3/Co_3O_4 photoanodes in 1 M Na_2S solution.

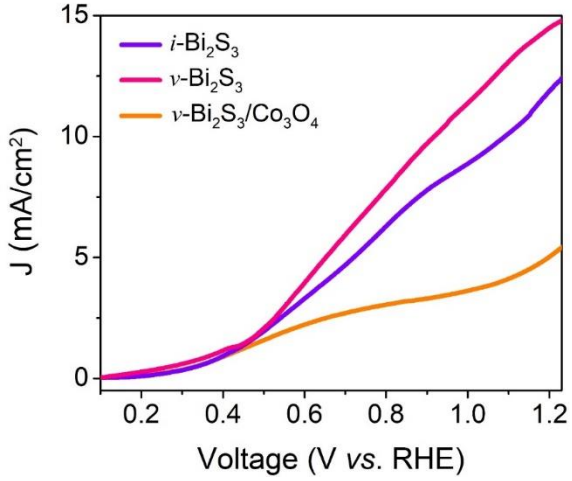

Fig. S8. (a) Electrochemical impedance spectra (EIS) Nyquist plots, (b) Open circuit potentials, (c) Steady-state photocurrent for the *i*-Bi_2S_3, *v*-Bi_2S_3, and *v*-Bi_2S_3/Co_3O_4 and (d) Amount of oxygen evolved from the *v*-Bi_2S_3/Co_3O_4 photoanode under an applied potential of 1.23 V versus RHE under AM1.5G simulated sunlight.

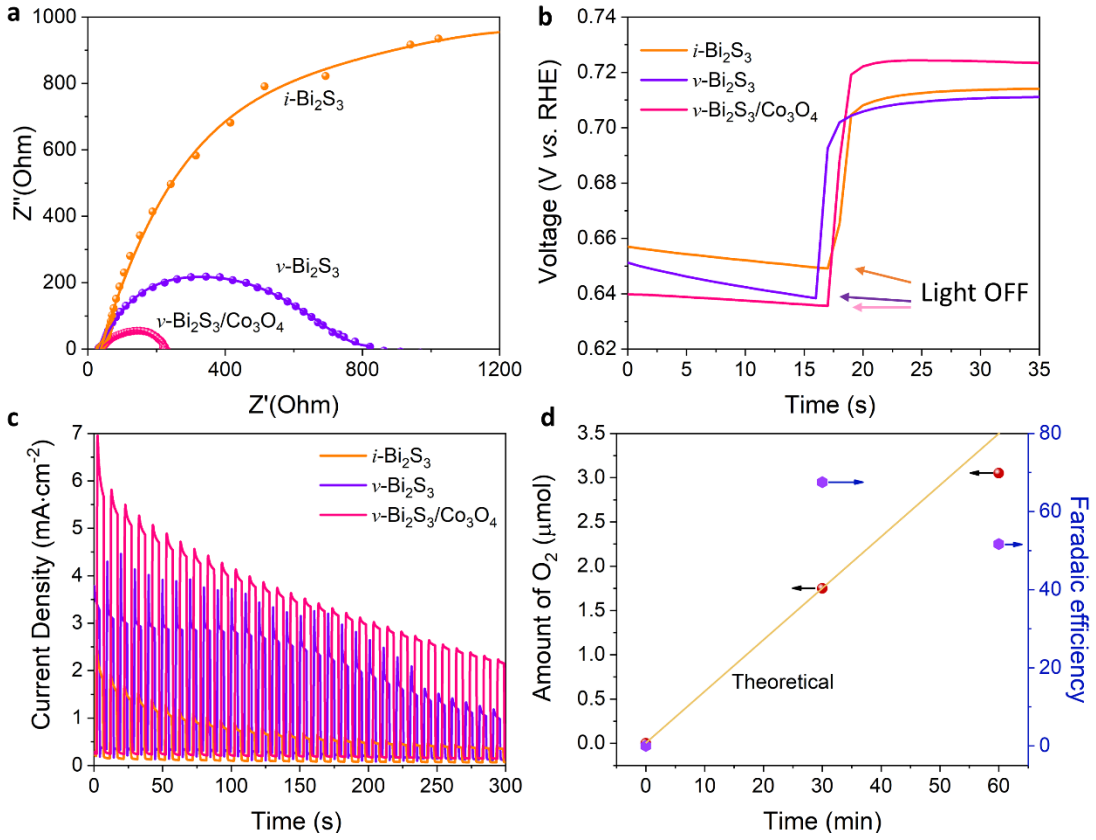

Fig. S9. Supplementary DFT calculation. (a) High symmetry points in the Brillouin zone of *v*-Bi_2S_3 before Co_3O_4 loading and (b) the corresponding calculated energy diagrams. *Note: The vacancy concentration is estimated from XPS analysis.*